

# SIMULATION OF MULTISCALE HYDROPHOBIC LIPID DYNAMICS VIA EFFICIENT INTEGRAL EQUATION METHODS\*

SZU-PEI P. FU<sup>†</sup>, ROLF RYHAM<sup>†</sup>, ANDREAS KLÖCKNER<sup>‡</sup>, MATT WALA<sup>‡</sup>, SHIDONG JIANG<sup>§</sup>, AND YUAN-NAN YOUNG<sup>§</sup>

**Abstract.** In this paper, a mathematical model for long-range, hydrophobic attraction between amphiphilic particles is developed to quantify the macroscopic assembly and mechanics of a lipid bilayer membrane in solvents. The nonlocal interactions between amphiphilic particles are obtained from the first domain variation of a hydrophobicity functional, giving rise to forces and torques (between particles) that dictate the motion of both particles and the surrounding solvent. The functional minimizer (that accounts for hydrophobicity at molecular-aqueous interfaces) is a solution to a boundary value problem of the screened Laplace equation. We reformulate the boundary value problem as a second-kind integral equation (SKIE), discretize the SKIE using a Nyström discretization and Quadrature by Expansion (QBX), and solve the resulting linear system iteratively using GMRES. We evaluate the required layer potentials using the GIGAQBx fast algorithm, a variant of the Fast Multipole Method (FMM), yielding the required particle interactions with asymptotically optimal cost. A mobility problem formulation supplies the motion for the rigid particles in a viscous fluid. The simulated fluid-particle systems exhibit a variety of multiscale behaviors over both time and length. Over short time scales, the numerical results show self-assembly for model lipid particles. For large system simulations, the particles form realistic configurations like micelles and bilayers. Over long time scales, the bilayer shapes emerging from the simulation appear to minimize a form of bending energy.

**Key words.** energy variation, integral equation method, lipid dynamics

**AMS subject classifications.** 31A10, 35A15, 92C05

**DOI.** 10.1137/18M1219503

**1. Introduction.** In recent years, researchers have developed various macroscopic continuum formulations and a number of numerical methods for calculating energy minimizing and time-dependent shapes of lipid bilayer membranes, vesicles, and red blood cells. While the Helfrich free energy of a lipid bilayer membrane assumes an infinitely thin membrane thickness [74, 33], many other continuum models incorporate more lipid physics [2, 6, 61] and membrane structures [12, 13, 21, 28, 43]. These refined continuum formulations are, in principle, capable of capturing topological changes of a lipid bilayer membrane, such as membrane fusion and fission. However, no simulations of membrane fusion or fission based on these refined formulations are available in the literature (to the best of our knowledge), possibly due to the numerical challenges of efficiently and accurately resolving structures on the scale of membrane thickness.

\*Received by the editors October 9, 2018; accepted for publication (in revised form) October 16, 2019; published electronically February 4, 2020.

<https://doi.org/10.1137/18M1219503>

**Funding:** The third and fourth authors were supported in part by NSF grants DMS-1418961 and DMS-1654756. The fifth author was supported by NSF grants DMS-1418918 and DMS-1720405, and by the Flatiron Institute, a division of the Simons Foundation. The sixth author was supported by NSF grants DMS-1412789 and DMS-1614863.

<sup>†</sup>Department of Mathematics, Fordham University, Bronx, NY 10458 (sfu17@fordham.edu, rryham@fordham.edu).

<sup>‡</sup>Department of Computer Science, University of Illinois at Urbana-Champaign, Urbana, IL 61801 (andreask@illinois.edu, wala1@illinois.edu).

<sup>§</sup>Department of Mathematical Sciences, New Jersey Institute of Technology, Newark, NJ 07102 (shidong.jiang@njit.edu, yyoung@njit.edu).

Changes in topology of bilayer membranes, as occur in bilayer membrane fusion, pore formation, and protein insertion, for example, involve the introduction of a hydrophobic fissure in the normally intact monolayer surface. Due to the relatively large tension of a hydrocarbon-water interface, the energy of a hydrophobic fissure can dominate the membrane's elastic energy, making it necessary to also take into account local interactions at the molecular level [22, 14]. Moreover, in many subcellular structures, membrane energies are dominant in high curvature regions only a few lipids wide [34, 82].

Based on these observations, we focus on topological changes with mesoscopic interactions in a semicontinuum framework where the lipids are coarse-grained into amphiphilic Janus-type particles while their interactions with each other and the solvents are described at a continuum level. This hybrid approach provides a bridge from microscopic molecular formulation to macroscopic continuum description of a lipid bilayer membrane. Furthermore, the continuum limit of our hybrid mesoscopic model may facilitate efficient numerical algorithms for simulating fusion/fission of lipid bilayer membranes of physically relevant membrane size and dynamic duration.

Modern molecular dynamics (MD) simulators (such as MARTINI [52] and LAMMPS [66]) have the advantage in that they resolve all relevant molecular details, and have been widely employed to simulate fully atomistic or coarse-grained lipid bilayer membranes based on pairwise interactions [11, 23, 37, 38, 52, 81]. Traditionally, MD numerical methods use explicit fluid particles such as coarse-grained water molecules and pairwise Lennard-Jones interactions. There is the disadvantage, though, that an enormous number of water molecules and long computation time are needed in MD simulations, and it remains a great challenge to compute the hydrodynamic interactions of the lipid membrane at micron size for durations long enough to make physical predictions. One way to mitigate long computation time is to compute hydrodynamic interactions using an implicit solvent and Stokesian dynamics [4].

In the present work, we propose a novel approach to lipid-lipid interactions called the hydrophobic attraction potential (HAP). Let  $\Omega$  be an open, exterior domain in  $\mathbb{R}^n$  representing water surrounding a collection of amphiphilic particles, e.g., lipids. For dispersed particles, the energy associated with hydrophobic interfaces behaves as a surface energy. When nearby, particles decrease their energy by aggregating and sequestering their hydrophobic interfaces from water. These interactions are well-described by the Ginzburg-Landau-type domain functional

$$(1.1) \quad \Phi(\Omega, f) = \gamma \min_{u \in \mathcal{A}} I[u],$$

where

$$(1.2) \quad I[u] = \int_{\Omega} \rho |\nabla u|^2 + \rho^{-1} u^2 dx.$$

Here  $\mathcal{A} = \{u \in W^{1,2}(\Omega) : u = f \text{ on } \Sigma\}$  is the admissible class and  $f$  with range  $[0, 1]$  is the hydrophobicity label for the water-particle interface  $\Sigma = \partial\Omega$ . The parameter  $\gamma > 0$  is interfacial tension. Its value in bilayers has been widely investigated in both numerical and theoretical studies [18, 24, 56, 65]. For a Lipschitz domain  $\Omega$  and for  $f$  the trace of a function in  $W^{1,2}(\Omega)$  [19], the existence of a unique minimizer to (1.1) is a straightforward consequence of the closest point theorem [46].

The scalar function  $u$  of (1.1) models disruption in the hydrogen bonding network [17, 53]. For a point  $x \in \Sigma$  representing a hydrophobic interface, molecular rotation is restricted and there  $u(x) = f(x) = 1$ . Conversely,  $u(x) = f(x) = 0$  at a point

$x \in \Sigma$  representing a hydrophilic interface where rotation is unrestricted. In the water region,  $u$  in (1.1) is a solution to the boundary value problem (BVP) of the screened Laplace equation:

$$(1.3) \quad \begin{cases} -\rho^2 \Delta u + u = 0 & \text{in } \Omega, \\ u(x) = f(x) & \text{on } \Sigma, \\ u(x) \rightarrow 0 & \text{as } x \rightarrow \infty. \end{cases}$$

Solutions  $u$  of (1.3) have a boundary layer of thickness  $\rho > 0$ . Thus disruption in hydrogen bonding modeled by (1.3) extends into the bulk with characteristic distance  $\rho$  [15, 54].

The hydrophobic force is the first variation of the functional  $\Phi$  with respect to the shape of the domain  $\Omega$ . The challenge in the present work is to compute the hydrophobic force between several bodies of arbitrary shape and configuration. Section 2 carries out the variation for rigid body motions, and this reduces to a set of boundary integrals for the hydrophobic forces and torques. For simulations, we utilize a boundary condition  $f$  representing surface portions of lipid tail and lipid head, and we adopt an excluded volume repulsion to avoid particle collisions in the many-body simulations. As an illustration, Figure 1 shows the self-assembly process for three Janus-type particles in a viscous fluid.

An important feature of the model is that the potential  $\Phi$  and its intermolecular forces and torques, in contrast to that of coarse-grained theories, do not arise from any pairwise potentials (see Appendix A). To leading order, the attraction between particle pairs predicted by (1.1) is in accord with experimental force-distance curves [17, 48, 54]. The functional (1.1), however, requires modification to account for subnanometer force oscillations observed in experiment, e.g., through the inclusion of higher order terms. Nevertheless, the HAP captures the essential features of amphiphile self-assembly, and the variational calculations and numerical methods generalize to more complicated domain functionals.

An essential principle for molecular or particle based approaches is to ensure that the total free energy accounting for lipid-lipid and lipid-water interactions gives rise to an equivalent elastic characterization of membranes as determined by experimental measurements [77, 78]. Section 3 examines the elasticity of bilayer particle configurations. We obtain physical quantities such as bending modulus, tilt modulus, and stretching modulus by setting up corresponding equilibrium simulations from continuum theory [41, 58, 76].

Section 4 formulates the mobility problem to calculate hydrodynamics from the hydrophobic stress. The dynamics for many-particle simulations yield physically reasonable time scales and configurations. For example, we can track the particle dynamics over the nanosecond range needed for rapid particle self assembly, up to the microseconds range where bilayer and micelle shapes evolve over a slower time scale [69, 70].

Calculating the particle dynamics requires rapid, on-the-fly solution of (1.3). In section 5, we present a new second-kind integral equation (SKIE) formulation for the BVP (1.3), derived from a representation of the solution in which the unknowns are only on the boundary  $\Sigma$ . In section 6, we describe an approach to applying a recently developed Quadrature by Expansion Fast Multipole Method (QBX-FMM) scheme for discretizing the SKIE accurately and adaptively, solving the resulting linear system, and evaluating the desired physical quantities afterwards accurately and rapidly. The resulting scheme has linear complexity with an optimal number of unknowns for the

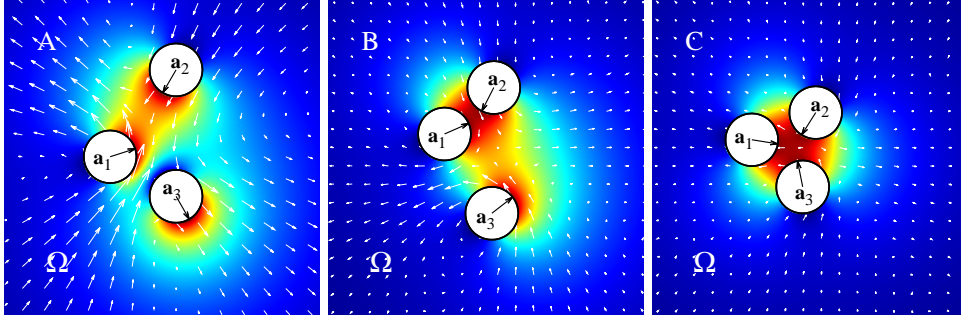


FIG. 1. The figure illustrates hydrophobic attraction of amphiphiles in a zero-Reynolds number fluid. The black arrows are the directors  $\mathbf{d}_i$  of the particles centered at  $\mathbf{a}_i$ ,  $i = 1, 2, 3$ . The white arrows are the fluid velocity. The color map has dark blue for  $u = 0$  (lipid heads) and dark red for the hydrophobic interface  $u = 1$  (lipid tails). Activity, shown as pseudocolor shading in the figure, extends from the hydrophobic interface into the bulk. Going from panels A to B, particles  $\mathbf{a}_1$  and  $\mathbf{a}_2$  come together and  $\mathbf{a}_3$  rotates counterclockwise. In panel C, the particles sequester activity to a single hydrophobic core. (Figure in color online.)

simulation of particle dynamics at each time step. To compare the computational cost against MD simulations, even solvent free coarse-grained models have at least  $O(N^2)$  complexity in the number of particles  $N$  [11, 60].

**2. Intermolecular forces and torques.** We calculate the first variation of  $\Phi$  with respect to rigid body deformations [1, 73]. Consider  $N$ -many, rigid particles represented by disjoint, bounded, closed regions  $P_1, P_2, \dots, P_N$  in  $\mathbb{R}^n$ ,  $n = 2, 3$ . The water region (the exterior domain) and particle-water interface are

$$(2.1) \quad \Omega = \mathbb{R}^n \setminus \bigcup_{i=1}^N P_i, \quad \Sigma = \bigcup_{i=1}^N \partial P_i,$$

respectively. Throughout,  $\nu$  denotes the unit outward normal to  $\Omega$ , and  $\nu_i$  denotes the unit outward normal to  $P_i$ . Note that  $\nu$  and  $\nu_i$  have opposite orientation, as illustrated in Figure 2. Suppose that  $u$  is the solution to the screened Laplace BVP (1.3) with the material label  $f$ . Then the force  $\mathbf{F}_i$  and torque  $\tau_i^0$  acting on particle  $P_i$  are

$$(2.2) \quad \mathbf{F}_i = \int_{\partial P_i} \mathbf{T} \cdot \nu_i dS, \quad \tau_i^0 = \int_{\partial P_i} \mathbf{r}_0 \times (\mathbf{T} \cdot \nu_i) dS,$$

where

$$(2.3) \quad \mathbf{T} = \gamma \rho^{-1} u^2 \mathbf{I} + 2\rho \gamma (\tfrac{1}{2} |\nabla u|^2 \mathbf{I} - \nabla u \otimes \nabla u)$$

is the hydrophobic stress and  $\mathbf{r}_0$  is the position vector relative to the origin  $\mathbf{0}$ . To ensure that (2.2) is well-defined and to guarantee differentiability of the domain functional, we assume that  $\Omega$  is a  $C^{2,\alpha}$  domain and that  $f = \tilde{f}$  on  $\Sigma$  for some  $\tilde{f} \in C^{2,\alpha}(\overline{\Omega})$ .

To compare  $\Phi(\Omega, f)$  against that of competing domains, consider a one-parameter family of rigid transformations

$$(2.4) \quad \mathbf{x}_i(\mathbf{X}, \epsilon) = \mathbf{c}_i(\epsilon) + \mathbf{Q}_i(\epsilon) \mathbf{X},$$

parametrized by  $\epsilon \in \mathbb{R}$ . The vector  $\mathbf{c}_i(\epsilon)$  and tensor  $\mathbf{Q}_i(\epsilon)$  give the displacement and rotation of the particle  $P_i$ ,  $i = 1, \dots, N$ , relative to the origin. They satisfy  $\mathbf{c}_i(0) = \mathbf{0}$

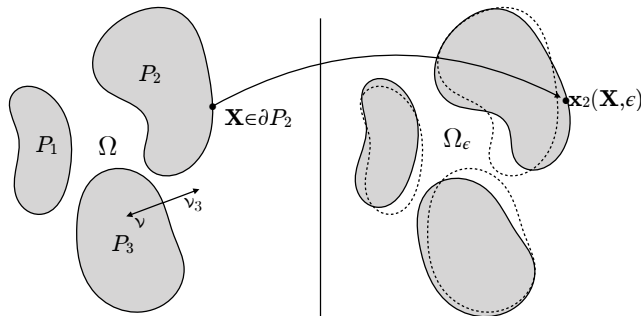


FIG. 2. On the left are three particles  $P_1$ ,  $P_2$ , and  $P_3$  forming the exterior domain  $\Omega$ . Rigid transformation of each particle (right panel) leads to the perturbed exterior domain  $\Omega_\epsilon$  and changes in the relative positions of the material label  $f_\epsilon$ , resulting in variations in the hydrophobic potential  $\Phi$ .

and  $\mathbf{Q}_i(0) = I$  so that  $\mathbf{x}_i(\mathbf{X}, 0)$  is the identity transformation;  $\mathbf{Q}_i(\epsilon)\mathbf{Q}_i^T(\epsilon) = I$  for all  $\epsilon$ . The distance between  $P_i$  and  $P_j$  is positive whenever  $i \neq j$ . Therefore, for  $\epsilon$  in an open interval about 0, let

$$(2.5) \quad \Omega_\epsilon = \mathbb{R}^n \setminus \bigcup_{i=1}^N \mathbf{x}_i(P_i, \epsilon), \quad \Sigma_\epsilon = \partial\Omega_\epsilon, \quad f_\epsilon(\mathbf{x}_i(\mathbf{X}, \epsilon)) = f(\mathbf{X}), \quad \mathbf{X} \in \partial P_i.$$

Finally, let  $u_\epsilon(x)$  be the one-parameter family of solutions to the perturbed BVP of screened Laplace equation

$$(2.6) \quad -\rho^2 \Delta u_\epsilon + u_\epsilon = 0 \text{ in } \Omega_\epsilon, \quad u_\epsilon = f_\epsilon \text{ in } \Sigma_\epsilon, \quad u_\epsilon \rightarrow 0 \text{ as } x \rightarrow \infty.$$

The domain  $\Omega_\epsilon$  and boundary  $\Sigma_\epsilon$  are the water region and water-molecule interface after transforming each particle according to its rigid motion (2.4) (see Figure 2). For  $x \in \Omega$ , let

$$\dot{u}(x) = \frac{d}{d\epsilon} u_\epsilon(x) \Big|_{\epsilon=0},$$

and extend  $\dot{u}$  continuously to  $\bar{\Omega}$ . Due to (2.5), we have the transport identity

$$(2.7) \quad \dot{u} + \nabla u \cdot \dot{\mathbf{x}} = 0 \text{ on } \Sigma,$$

where  $\dot{\mathbf{x}}(\mathbf{X}) = \frac{d\mathbf{x}_i}{d\epsilon}(\mathbf{X}, 0)$  whenever  $\mathbf{X} \in P_i$ . (Note, however, that the values of  $\dot{u}$  in  $\Omega$  are determined by the BVP (2.6), and, therefore, do not generally satisfy this transport relation.)

Applying the Reynolds transport theorem [47], we obtain

$$(2.8) \quad \begin{aligned} \frac{d}{d\epsilon} \Phi(\Omega_\epsilon, f_\epsilon) \Big|_{\epsilon=0} &= \gamma \frac{d}{d\epsilon} \left( \int_{\Omega_\epsilon} \rho |\nabla u_\epsilon|^2 + \rho^{-1} u_\epsilon^2 dx \right) \Big|_{\epsilon=0} \\ &= \gamma \int_{\Omega} 2\rho \nabla u \cdot \nabla \dot{u} + 2\rho^{-1} u \dot{u} dx + \gamma \int_{\Sigma} (\rho |\nabla u|^2 + \rho^{-1} u^2) \dot{\mathbf{x}} \cdot \nu dS. \end{aligned}$$

Integration by parts then gives

$$(2.9) \quad \frac{d}{d\epsilon} \Phi(\Omega_\epsilon, f_\epsilon) \Big|_{\epsilon=0} = \gamma \int_{\Sigma} (\rho |\nabla u|^2 + \rho^{-1} u^2) \dot{\mathbf{x}} \cdot \nu - 2\rho \nabla u \cdot \nu \dot{u} dS.$$

Due to the minimality condition  $-\rho^2 \Delta u + u = 0$ , the interior values of  $u$  do not enter (2.9). Based on (2.7) and the fact that  $\nu$  and  $\nu_i$  have opposite orientation,

$$\begin{aligned}
 \frac{d}{d\epsilon} \Phi(\Omega_\epsilon, f_\epsilon) \Big|_{\epsilon=0} &= \gamma \sum_{i=1}^N \int_{\partial P_i} -(\rho |\nabla u|^2 + \rho^{-1} u^2) \nu_i \cdot \dot{\mathbf{x}}_i(0) + 2\rho \nabla u \cdot \nu_i \nabla u \cdot \dot{\mathbf{x}}_i(0) dS \\
 &= \gamma \sum_{i=1}^N \int_{\partial P_i} \dot{\mathbf{x}}_i(0) \cdot \left[ -\rho^{-1} u^2 \mathbf{I} + 2\rho (\nabla u \otimes \nabla u - \frac{1}{2} |\nabla u|^2 \mathbf{I}) \right] \cdot \nu_i dS \\
 &= - \sum_{i=1}^N \int_{\partial P_i} (\dot{\mathbf{c}}_i(0) + \dot{\mathbf{Q}}_i(0) \mathbf{r}_0) \cdot \mathbf{T} \cdot \nu_i dS \\
 (2.10) \quad &= - \sum_{i=1}^N (\dot{\mathbf{c}}_i(0) \cdot \mathbf{F}_i + \mathbf{w}_i \cdot \tau_i^0),
 \end{aligned}$$

where  $\mathbf{w}_i = \langle w_1^i, w_2^i, w_3^i \rangle$  is the axial vector for the skew symmetric tensor  $\dot{\mathbf{Q}}_i(0)$ . In the second-to-last equation, the minus sign makes the force act in the negative direction of the potential gradient. This establishes (2.2) and (2.3).

In the formulation (2.4), the rigid motions are independent. Consider the case when the rigid motions are uniform, that is,  $\mathbf{c}_i(\epsilon) = \mathbf{c}(\epsilon)$  and  $\mathbf{Q}_i(\epsilon) = \mathbf{Q}(\epsilon)$  for all  $i = 1, \dots, N$ . Then the solution to the perturbed BVP (2.5), (2.6) satisfies

$$(2.11) \quad u_\epsilon(\mathbf{c}(\epsilon) + \mathbf{Q}(\epsilon)\mathbf{X}) = u(\mathbf{X}).$$

It follows that  $\Phi(\Omega_\epsilon, f_\epsilon) = \Phi(\Omega, f)$  for all  $\epsilon$  and, by (2.10), that

$$(2.12) \quad \sum_{i=1}^N \dot{\mathbf{c}}_i(0) \cdot \mathbf{F}_i + \mathbf{w} \cdot \tau_i^0 = -\frac{d}{d\epsilon} \Phi(\Omega_\epsilon, f_\epsilon) \Big|_{\epsilon=0} = -\frac{d}{d\epsilon} \Phi(\Omega, f) \Big|_{\epsilon=0} = 0.$$

Here,  $\mathbf{w} = \langle w_1, w_2, w_3 \rangle$  is the axial vector for  $\dot{\mathbf{Q}}(0)$ . Since  $\dot{\mathbf{c}}(0)$  and  $\mathbf{w}$  are arbitrary, we have

$$(2.13) \quad \sum_{i=1}^N \mathbf{F}_i = \mathbf{0}, \quad \sum_{i=1}^N \tau_i^0 = \mathbf{0}.$$

In other words, the net hydrophobic interaction is force and torque free.

**2.1. Simulations.** For the simulations in this paper, the  $P_1, \dots, P_N$  are two-dimensional Janus-type particles. The direction vector  $\mathbf{d}_i = \langle \cos \theta_i, \sin \theta_i \rangle$  specifies orientation and  $\mathbf{a}_i$  is the particle position (e.g., the center of mass, Figure 1). The particle shapes are ellipses with semimajor and semiminor axes  $a_i$  and  $b_i$ , respectively. In the case of lipids,  $2a_i$  represents lipid length, and the major axis is parallel to the director and hydrocarbon tail.

The material label for the Janus-type particle takes the form

$$(2.14) \quad f(\mathbf{x}) = 1 - \sin^p(\theta), \quad \mathbf{x} \in \partial P_i,$$

where  $\theta$  is the angle formed by  $\mathbf{x} - \mathbf{a}_i$  and  $\mathbf{d}_i$ . Accordingly, there is a smooth transition in hydrophobicity across the particle [51], with the boundary portion in the direction  $\mathbf{d}_i$  modeling a hydrophobic tail and the opposite boundary portion modeling a hydrophilic head. The size of the hydrophobic region grows with the even integer parameter  $p$ . Finally,

$$(2.15) \quad \tau_i = \tau_i^0 - \mathbf{a}_i \times \mathbf{F}_i$$

is the two-dimensional (scalar) torque about the position  $\mathbf{a}_i$ .

For small but fixed separations between particles, our numerical scheme accurately resolves the field  $u$  without an undue cost increase due to refinement; we postpone a detailed discussion of the method and involved cost to section 6. Dynamically, the forces (2.2) bring the coarse-grained lipid particles into contact. An excluded volume repulsion prevents near-contact between particles [64]. For two circular particles, the interaction is

$$(2.16) \quad \mathbf{F}_{ij}^{\text{rep}} = c_0 \frac{q}{(|\mathbf{a}_i - \mathbf{a}_j| - (b_i + b_j))^{q+1}} \frac{\mathbf{a}_i - \mathbf{a}_j}{|\mathbf{a}_i - \mathbf{a}_j|}, \quad i \neq j.$$

We fix the order  $q = 3$  ( $q = 4$  in three dimensions) and use the parameter  $c_0$  to control the strength of repulsion. For ellipses of eccentricity close to zero, we approximate the excluded volume repulsion using three circular particles placed along the major axes, as described in the supplementary material file Supplementary.pdf [local/web 394KB], section SM1. In what follows,

$$(2.17) \quad \mathbf{F}_i^{\text{rep}}, \quad \tau_i^{\text{rep}}, \quad \Phi_{\text{rep}}$$

denote the excluded volume force, torque, and repulsion potential, respectively. The total potential that includes hydrophobic attraction and steric repulsion is

$$(2.18) \quad \Phi_{\text{Total}} = \Phi + \Phi_{\text{rep}}.$$

For the simulations, we assume translation invariance in the  $z$ -direction. Figures 5 and 8 give values in  $k_B T$  per length since the two-dimensional simulations are for the cross-section of a three-dimensional bilayer. All other physical parameters correspond to their usual three-dimensional value.

We use  $2a_i = 2.5$  nm as a representative phospholipid length [3], the screening length  $\rho = 2.5$  nm [17, 48, 63, 35, 76], and  $c_0 = 0.5$  pN nm<sup>4</sup> for the interparticle repulsion. Bilayers containing different single pure components give various values of interfacial tension  $\gamma$  which fall within the range of 0.7–5.3 pN nm<sup>−1</sup> [45, 65]. We find that the mechanical moduli calculated from our simulation data are in good agreement with results in the experimental literature when the interfacial tension  $\gamma = 4.1$  pN nm<sup>−1</sup>. Coincidentally, this value corresponds to a specific lipid composition DPoPC:SM:Chol in a bilayer membrane [24, Table 1].

Our experiences show that the computational cost to maintain the same numerical accuracy in solving the BVP (1.3) grows only moderately when going from circular to elliptical model particles. For instance, ellipses with  $a_i/b_i = 3$  require 60% more grid points than for  $a_i/b_i = 1$ . At the same time, ellipses afford flexibility in terms of dimensions that determine physical properties of a bilayer. However, we remark that rather than representing a physical lipid or collection of lipids, the model particle discretizes the mean lipid position and orientation but without the mesh associated with finite element methods; see, for example, [2, 72]. Similarly, the gap region between neighboring particles indicates a hydrophobic zone and not an intervening water.

**3. Bilayer elasticity.** We compare our two-dimensional equilibrium configurations to those found in membrane continuum mechanics. In large particle number HAP simulations, particles bring opposing hydrophobic regions into contact, forming two abutting monolayers of a bilayer. Continuum theory describes monolayers using

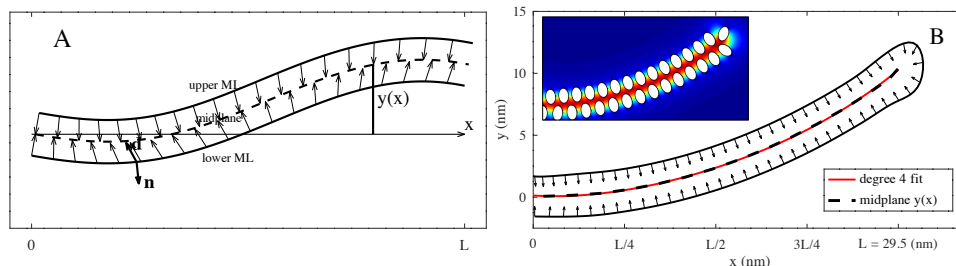


FIG. 3. Panel A depicts a bilayer, with its upper and lower monolayers (solid curves) and midplane (dashed curve). The director field  $\mathbf{d}$  points in the direction of the lipid tails and the normal  $\mathbf{n}$  points outward from bilayer core. When deformations and tilt are small ( $|y'| \ll 1$ ,  $|\mathbf{d} \times \mathbf{n}| \ll 1$ ) energy is quantified in terms of the midplane height function  $y(x)$ . Panel B has the Janus-type amphiphilic particles with uniform loading and a clamped boundary condition. Fitting (3.4) to the midplane (dashed curve) yields the bending modulus  $k_B = 8.51 k_B T$ . In panel B (inset), enumerating counterclockwise from the bottom left, particles satisfy  $x_1 = 0$ ,  $x_{16} = 1.5$ ,  $\theta_1 = \pi/2$ ,  $\theta_{16} = -\pi/2$ , and  $y_1 = 0$ . The parameters are  $\gamma = 4.1 \text{ pN nm}^{-1}$ ,  $\rho = 2.5 \text{ nm}$ ,  $c_0 = 0.5 \text{ pN nm}^{-4}$ , and  $k = 0.0116 \text{ pN nm}^{-2}$ . The ellipses have  $a_i = 1.25 \text{ nm}$  and  $b_i = 0.8 \text{ nm}$ .

a director field  $\mathbf{d}$  to track lipid orientations, along with a field  $\mathbf{n}$  given by the monolayer surface normal (Figure 3A), and quantifies monolayer energy using a Helfrich Hamiltonian

$$(3.1) \quad \int_C \frac{1}{2} k_B \left[ (\text{Div } \mathbf{d} + k_0)^2 - k_0^2 \right] + \frac{1}{2} k_\theta |\mathbf{d} \times \mathbf{n}|^2 ds.$$

The curve  $C$  tracks the cross-section of the monolayer neutral surface. The integrand in (3.1) contains the splay distortion  $\text{Div } \mathbf{d}$  with bending modulus  $k_B$ , and the tilt deformation  $\mathbf{d} \times \mathbf{n}$  with tilt modulus  $k_\theta$  [57]. The parameter  $k_0$  is a spontaneous curvature [71, 42, 75]. Since we are assuming translational invariance in the  $z$ -direction, the twist  $\text{Curl } \mathbf{d}$  and saddle-splay  $\det D$  distortions are absent from [33, 76], and (3.1) behaves as an energy density per length.

Consider a planar bilayer subject to a uniform vertical load. The bilayer is clamped and horizontal at one end, and the restoring force of bending in the free part of the bilayer opposes the load. Taking  $\mathbf{d}$  parallel to  $\mathbf{n}$  and assuming a small deformation gives the appropriate functional

$$(3.2) \quad \int_0^L k_B (y'')^2 - ky dx, \quad y(0) = y'(0),$$

where  $y(x)$  is the height function for the bilayer midplane (Figure 3A, dashed curve),  $\text{Div } \mathbf{d} = \pm y''$ , and  $k$  is the load strength. The summation of the monolayer energies (3.1) with opposite normals leads to the cancellation of the spontaneous curvature terms.

Minimizers of (3.2) satisfy the BVP

$$(3.3) \quad 2k_B y^{(4)} = k, \quad y(0) = y'(0) = y''(L) = y^{(3)}(L) = 0.$$

We find the solution

$$(3.4) \quad y(x) = \frac{kL^4}{2k_B} \left[ \frac{1}{24} \left( \frac{x}{L} \right)^4 - \frac{1}{12} \left( \frac{x}{L} \right)^3 + \frac{1}{4} \left( \frac{x}{L} \right)^2 \right].$$



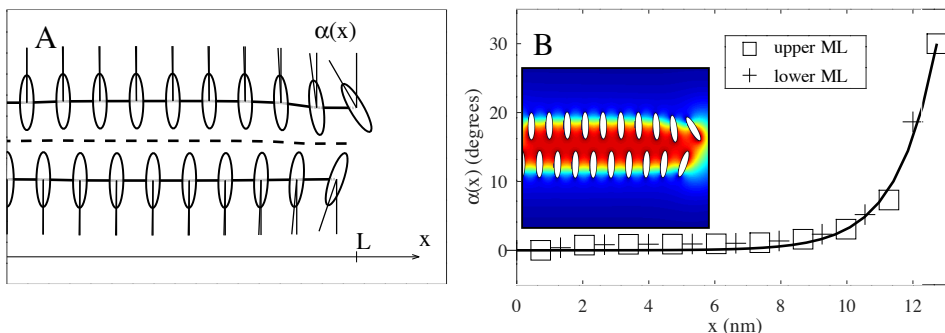


FIG. 4. The monolayers in panel A are flat and the tilt is nonzero. The horizontal coordinate  $x$  runs between 0 and the length of bilayer,  $L$ , and the function  $\alpha(x)$  measures the angle between  $-\mathbf{d}$  and the unit normal. The boundary conditions for (3.6) are  $\alpha_0 = 0^\circ$  and  $\alpha_1 = 30^\circ$ . In panel B, the  $+$  and  $\square$  symbols are the angles at the particle centers. The parameters are  $\gamma = 4.1 \text{ pN nm}^{-1}$ ,  $\rho = 2.5 \text{ nm}$ ,  $c_0 = 0.5 \text{ pN nm}^{-4}$ , and  $k = 0.0116 \text{ pN nm}^{-2}$ . The ellipses have  $a_i = 1.25 \text{ nm}$  and  $b_i = 0.3125 \text{ nm}$ .

Thus, we can determine  $k_B$  from curves of the form (3.4) whenever  $L$  and  $k$  are given.

The inset in Figure 3B shows a HAP equilibrium configuration used to determine  $k_B$ . The  $N = 30$  particles minimize the modified functional

$$(3.5) \quad \Phi_{\text{Total}} - \sum_{i=1}^N \tilde{k} y_i,$$

where the  $\tilde{k} = Lk/N$  is the discrete load strength coming from quadrature of the integral (3.2) with  $N$  many particles. To achieve minimality, the particles start in the shape of a flat bilayer, and then migrate upward following steepest gradient descent for (3.5).

The main figure in Figure 3B depicts the monolayer neutral surface (solid curve), midplane (dashed curve), and the lipid directors interpolated from the discrete particle positions and orientations (of the inset). The directors are normal everywhere to the neutral surface, and the deformations are small. This justifies applying the zero-tilt, small-deformation solution (3.4). Fitting a fourth degree polynomial to the midplane curve (Figure 3B, red curve) supplies the coefficient  $(kL^4/2k_B)$  of (3.4). Combining the coefficient with simulation values for  $L$  and  $k$  (Figure 3B, caption) yields  $k_B = 8.51 \text{ k}_B\text{T}$ . This value for the bending modulus is for ellipses using  $p = 6$  in the hydrophobicity boundary condition (2.14). To assess how bilayer rigidity depends on the material label, we considered the energy minimization with  $p = 2$ , which gave  $k_B = 13.54 \text{ k}_B\text{T}$ . We conclude that under HAP, particle configurations behave like an elastic material. The associated bending modulus grows with symmetry in the hydrophobic surface label, e.g.,  $k_B$  was largest for  $p = 2$  where the label is symmetric across  $\theta = \pi/2$ .

Now we consider a flat monolayer with nonzero tilt (Figure 4A). The splay distortion comes from changes in the angle  $\alpha(x)$  between the director  $\mathbf{d}$  and the vertical. For small angles, the monolayer energy (3.1) becomes

$$(3.6) \quad \int_0^L \frac{1}{2} k_B (\alpha')^2 + \frac{1}{2} k_\theta \alpha^2 dx, \quad \alpha(0) = \alpha_0, \quad \alpha(L) = \alpha_1.$$

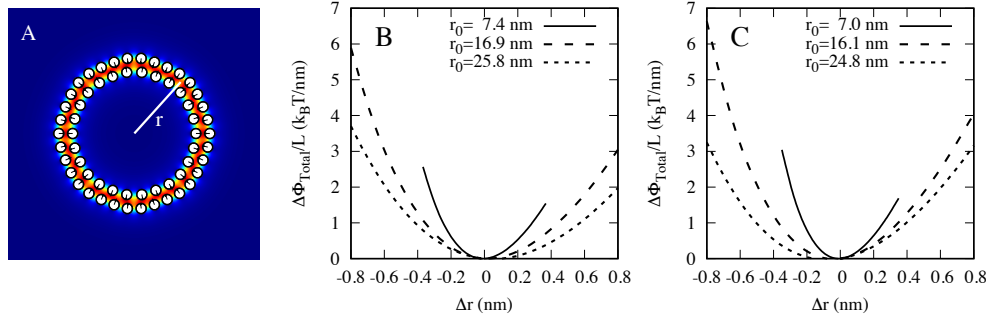


FIG. 5. Panel A shows the activity field for the cross-section of a cylindrical bilayer. The radius measures from the center to the midplane. Panels B and C plot the change in energy  $\Delta\Phi_{\text{Total}} = \Phi_{\text{Total}}(r) - \Phi_{\text{Total}}(r_0)$  per length of the cylinder under stretching and compression:  $\Delta r = r - r_0$ . Equilibrium radius  $r_0$  decreases with  $c_0$ ; the curves are for  $c_0 = 0.5 \text{ pN nm}^4$  in panel B, and  $c_0 = 0.25 \text{ pN nm}^4$  in panel C ( $\gamma = 4.1 \text{ pN nm}^{-1}$ , in both panels). The solid, dashed, and dotted curves use  $N = 26$ ,  $N = 60$ , and  $N = 92$  particles, and collapse onto a single curve when multiplied by  $r_0$ .

Note that we have left off the null-Lagrangian term  $k_B k_0 \alpha'$  from this expression since  $k_B$ ,  $k_0$ , and the boundary data  $\alpha_0$  and  $\alpha_1$  are constants. Assuming  $\alpha(0) = 0$ , minimizers of (3.6) take the form

$$(3.7) \quad \alpha(x) = \alpha_1 \frac{\sinh(x/\kappa)}{\sinh(L/\kappa)},$$

where  $\lambda = \sqrt{k_B/k_\theta}$  is the tilt decay length [45]. Figure 4B shows the data (plusses and squares) for the HAP equilibrium configuration with fixed endpoint angles. The solid curve fits (3.7) to the angle data for the value  $\lambda = 1.2 \text{ nm}$ . This value is consistent with experimental and theoretical measurements of the bending and tilt moduli [57, 41].

In HAP, tilt dissipation is a consequence of repulsion between rod-like particles. The ellipses in Figure 4 are elongated and have  $a_i/b_i = 4$ . When the particles are more circular ( $a_i/b_i \sim 1$ ), the bulk particles ignore endpoint orientations and the angle function  $\alpha(x)$  is nonmonotonic in  $x$ .

Finally, we discuss simulation data for stretching. Consider the stretching energy of a cylindrical bilayer:

$$(3.8) \quad k_A \frac{(A - A_0)^2}{A_0},$$

where  $A = 2\pi rL$ ,  $r$  is the midplane radius,  $L$  is the cylinder length (in the  $z$ -direction), and  $A_0$  is the area at rest. The stretching modulus  $k_A$  is for a single monolayer, and (3.8) accounts for the energy of the inner and outer monolayer leaflets of the cylinder. Manipulation experiments give  $k_A$  in the range  $30\text{--}40 \text{ k}_B\text{T nm}^{-2}$  [56, 57].

To measure a stretching modulus, we form the circular cross-section of a cylinder of radius  $r$  (Figure 5A). The equilibrium shape is nearly circular (so long as there is a consistent number of particles in each leaflet), and the shape obtains an equilibrium radius  $r_0$  once compression and attraction are in balance. We use a harmonic bond to move  $r$  away from equilibrium and record the change in energy (Figure 5BC).

The three curves in Figure 5B collapse onto a single curve when multiplied by  $r_0$ . Fitting to  $cr_0(r - r_0)^2$  and comparing with (3.8) yields  $k_A = 33.4 \text{ k}_B\text{T nm}^{-2}$ ,  $35.3 \text{ k}_B\text{T nm}^{-2}$ , and  $35.9 \text{ k}_B\text{T nm}^{-2}$  for the three radii, respectively. The proximity of

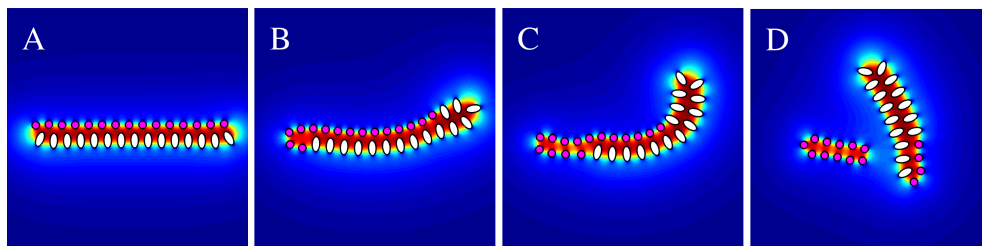


FIG. 6. Panels A–D show the spontaneous sorting and eventual fission of a planar bilayer mixture of small circular particles (magenta) and elliptical particles (white). The monolayer consisting of smaller, circular particles spontaneously migrates from the bilayer edge, and eventually breaks off, forming its own bilayer. The bending in panels B and C suggests that the smaller, circular particles have a spontaneous curvature more negative than for the larger, elliptical particles. The parameters are  $\gamma = 4.1 \text{ pN nm}^{-1}$ ,  $\rho = 2.5 \text{ nm}$ , and  $c_0 = 0.5 \text{ pN nm}^{-4}$ . The ellipses have  $p = 6$ ,  $a_i = 1.25 \text{ nm}$ , and  $b_i = 0.6225 \text{ nm}$ , while the circles have  $p = 2$ ,  $a_i = b_i = 0.6225 \text{ nm}$ . (Figure in color online.)

these three values suggests that HAP possesses a stretching modulus independent of particle number. Moreover, the attraction  $\gamma = 4.1 \text{ pN nm}^{-1}$  and repulsion parameters  $c_0 = 0.5 \text{ pN nm}^4$  yield a consistent and physically realistic stretching modulus, around  $k_A = 35 \text{ k}_B\text{T nm}^{-2}$ . As an illustration, the curves in Figure 5C are for the same tension parameter and half the repulsion strength. There is an overall reduction in the equilibrium radii with the decreased repulsion, and an increase in the stretching moduli  $k_A$  to  $40.310 \text{ k}_B\text{T nm}^{-2}$ ,  $40.083 \text{ k}_B\text{T nm}^{-2}$ , and  $39.393 \text{ k}_B\text{T nm}^{-2}$  for the three curves, respectively.

HAP yields physically realistic continuum-like bilayer morphologies, and these particle configurations possess elastic properties of lipid bilayer. The HAP can also handle topological changes and mixtures in a straightforward manner. Figure 6 illustrates the gradient descent dynamics of a lipid mixture between small, circular and large, elliptical particles. Under hydrophobic attraction and excluded volume repulsion, the particle mixture segregates into two bilayers of more uniform composition. Diffusive interface and level-set approaches have dealt with the problem of mixtures by defining transport equations for each lipid species density [49, 55, 25].

Hemifusion is one of the key intermediates of membrane fusion involving a Y-shaped junction between three bilayers [9, Figure 8, Panel C]. Pioneering work by Promilso and coworkers [12, 13] has lead to functionalized Cahn–Hilliard, diffusive interface energies that exhibit freestanding elastic phases, including the Y-shaped junction [43, 21]. It is still unclear whether the HAP formulation of the present work is more or less efficient than a functionalized Cahn–Hilliard approach for capturing the granular energetic details of fusion [72].

**4. Hydrodynamics of amphiphilic particles in a viscous solvent.** To define particle velocities, we assume that the amphiphilic particles are immersed in an incompressible viscous fluid in the Stokes flow regime. Then all of the particles interact with one another through both hydrophobic forces and Stokesian hydrodynamic interactions. The two-dimensional particles  $P_i$  have the translational and angular velocities

$$(4.1) \quad \frac{d\mathbf{a}_i}{dt} = \mathbf{v}_i, \quad \frac{d\theta_i}{dt} = \omega_i,$$

$i = 1, \dots, N$ . For the amphiphilic particles in a solvent, the forces  $\mathbf{F}_i$ ,  $\mathbf{F}_i^{\text{rep}}$  and torques  $\tau_i$ ,  $\tau_i^{\text{rep}}$  are calculated from (2.2) and (2.15), respectively. The velocities  $\mathbf{v}_i$  and  $\omega_i$  are

coupled together through the fluid velocity  $\mathbf{u}$  and pressure  $p$  satisfying

$$(4.2) \quad \begin{aligned} -\mu\Delta\mathbf{u} + \nabla p &= 0, \\ \nabla \cdot \mathbf{u} &= 0 \quad \text{in } \Omega, \\ \mathbf{u} &\rightarrow 0 \quad \text{as } |\mathbf{x}| \rightarrow \infty, \\ \mathbf{u}(\mathbf{x}) &= \mathbf{v}_i + \omega_i(\mathbf{x} - \mathbf{a}_i)^\perp, \quad \mathbf{x} \in \partial P_i, \end{aligned}$$

with fluid viscosity  $\mu$  and subject to the stress balance conditions

$$(4.3) \quad \int_{\partial P_i} \mathbf{S} \cdot \mathbf{n} dS = \mathbf{F}_i + \mathbf{F}_i^{\text{rep}}, \quad \int_{\partial P_i} (\mathbf{x} - \mathbf{a}_i) \times \mathbf{S} \cdot \mathbf{n} dS = \tau_i + \tau_i^{\text{rep}}.$$

Here  $\mathbf{S}$  is the Newtonian stress tensor. From (2.13) these particle forces and torques also satisfy the force-free and torque-free conditions, guaranteeing the existence of an integral solution for the many-body mobility problem. The evolution equations (4.1)–(4.3) satisfy the dissipation relation [47]

$$(4.4) \quad \frac{d}{dt} \Phi_{\text{Total}} + \int_{\mathbb{R}^n} \frac{1}{2} \mu |\nabla \mathbf{u} + \nabla \mathbf{u}^T|^2 dx = 0.$$

In two dimensions, the kernels of single and double layer potentials for solving the Stokes equation are the stokeslet and stresslet

$$(4.5) \quad \begin{aligned} G_{i,j}^{\text{Stokeslet}}(\mathbf{x}, \mathbf{y}) &= \frac{1}{4\pi\mu} \left[ \log |\mathbf{x} - \mathbf{y}| \delta_{ij} + \frac{(x_i - y_i)(x_j - y_j)}{|\mathbf{x} - \mathbf{y}|^2} \right], \\ \mathbf{T}_{i,j,k}^{\text{Stresslet}}(\mathbf{x}, \mathbf{y}) &= -\frac{1}{\pi\mu} \frac{(x_i - y_i)(x_j - y_j)(x_k - y_k)}{|\mathbf{x} - \mathbf{y}|^4}, \end{aligned}$$

respectively, with  $i, j, k = 1, 2$ . For a velocity surface density  $\boldsymbol{\mu}$ , the stresslet satisfies the jump across the boundary

$$(4.6) \quad \lim_{\mathbf{z} \rightarrow \mathbf{x}^\pm} \mathbf{f}_{i,\pm}(\mathbf{z}) = \mp \frac{1}{2} \boldsymbol{\mu}_i(\mathbf{x}) + \text{p.v.} \int_{\partial P_i} \mathbf{T}_{i,j,k}^{\text{Stresslet}}(\mathbf{x}, \mathbf{y}) \boldsymbol{\mu}_j(\mathbf{y}) ds_{\mathbf{y}},$$

where  $\mathbf{f}_i$  denotes the surface traction of particle  $P_i$ . Following [67], one views the external force and torque due to hydrophobic attraction as an incident field with stress (2.3). The scattered field is then the net force and torque due to fluid mobility. If we split densities into  $\boldsymbol{\sigma}^{\text{inc}}(\mathbf{x}) = \{\boldsymbol{\sigma}_1^{\text{inc}}, \dots, \boldsymbol{\sigma}_N^{\text{inc}}\}$  and  $\boldsymbol{\mu}(\mathbf{x}) = \{\boldsymbol{\mu}_1, \dots, \boldsymbol{\mu}_N\}$ , then the particle dynamics (4.7) can be obtained by evaluating a single layer potential for corresponding densities  $\boldsymbol{\sigma}$  and  $\boldsymbol{\mu}$ .

$$(4.7) \quad \begin{aligned} \mathbf{u}(\mathbf{x}) &= \sum_{j=1}^N \int_{\partial P_j} G_{i,j}^{\text{Stokeslet}}(\mathbf{x}, \mathbf{y}) [\boldsymbol{\sigma}_j^{\text{inc}} + \boldsymbol{\mu}_j](\mathbf{y}) ds_{\mathbf{y}} \\ &= \mathbf{v}_i + \omega_i(\mathbf{x} - \mathbf{a}_i)^\perp \quad \forall \mathbf{x} \in \partial P_i, \end{aligned}$$

where

$$(4.8) \quad \begin{aligned} \mathbf{v}_i &= \frac{1}{|\partial P_i|} \int_{\partial P_i} \mathbf{u}(\mathbf{y}) ds_{\mathbf{y}}, \quad |\partial P_i| = \int_{\partial P_i} ds_{\mathbf{y}}, \\ \omega_i &= \tau^{-1} \int_{\partial P_i} (\mathbf{y} - \mathbf{a}_i) \times \mathbf{u}(\mathbf{y}) ds_{\mathbf{y}}, \quad \tau = \int_{\partial P_i} |\mathbf{y} - \mathbf{a}_i|^2 ds_{\mathbf{y}}. \end{aligned}$$

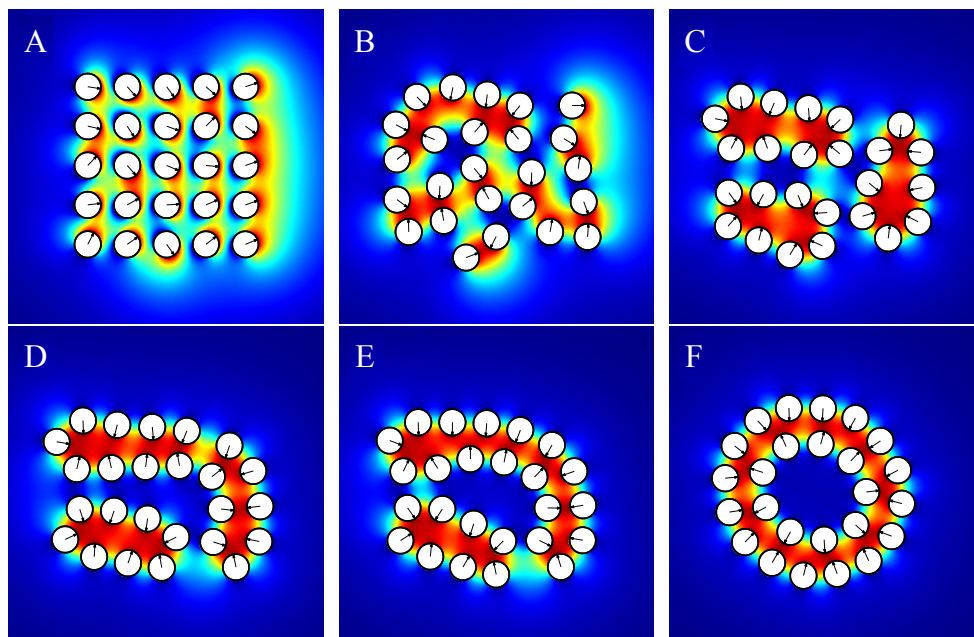


FIG. 7. For large system simulations, particles self-assemble into bilayer-like shapes and then eventually a cylindrical bilayer. Panels A–F are for 0, 3.8, 19, 76, 114, and 228 ns, respectively; step size  $\Delta T = 1.0[T] \approx 0.38$  ns. The configuration in panel F evolves very slowly to one that is slightly more circular.

For the time-marching scheme, we solve the mobility problem for the particle translation and rotation velocities. We then update the particle centers and orientations using a forward Euler scheme. Algorithm 5.1 provides the time-marching details.

Nondimensionalizing (1.1) with characteristic length 1.25 nm, fluid viscosity  $\mu = 1$  cP, and interfacial tension  $\gamma = 4.1$  pN nm<sup>-1</sup> gives the characteristic time  $[T] = \mu a / \gamma \approx 3.82 \times 10^{-10}$  s. As an illustration, the evolution in Figure 1 is for 100 time steps with time step size  $\Delta T = 1.0[T]$ . The time for self-assembly of a few particles from an initially random configuration is thus on the order of a nanosecond. This is consistent with times scales for lipid rearrangements in MD simulation [10]. Supplementary material movie file N3.mp4 [local/web 914KB] shows the self-assembly process for three particles.

Bilayer configurations form when we increase the number of particles in the simulation. Figure 7A has 25 Janus-type particles placed on a square grid. The initial orientations  $\theta_i$  are normally distributed about  $\theta = 0$ . Within ten time steps (Figure 7B), the particles rapidly rotate to pair their hydrophobic interfaces with that of neighboring particles. Pairings continue to merge, forming groups of eight or nine particles (Figure 7C). These groups stack together to form an arched bilayer shape resembling the cross-section of a stomatocyte (Figure 7E). Figure 7F clearly shows an inner and an outer monolayer configuration of a cylindrical bilayer.

Supplementary material movie file N25.mp4 [local/web 4.01MB] illustrates the self-assembly process for Figure 7A–F. As part of the computational complexity test, we have calculated particle dynamics for larger systems, and supplementary material movie file N100.mp4 [local/web 22.5MB] shows the results for 100 particles.

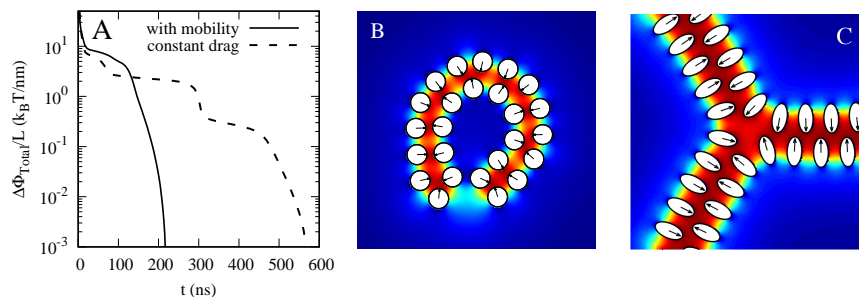


FIG. 8. Panel A plots the change in energy  $\Phi$  per length (solid curve) for the evolution Figure 7A–F. The initial rapid decrease over  $0 \text{ ns} < t < 10 \text{ ns}$  corresponds to Figure 7A–B. The moderate decrease over  $10 \text{ ns} < t < 150 \text{ ns}$  is for Figure 7C–E. Energy decreases very slowly over  $150 \text{ ns} < t < 600 \text{ ns}$ , where the bilayer evolves from a somewhat elliptical cross-section (Figure 7F) to one that is almost perfectly circular. The dashed curve gives corresponding values for a constant drag coefficient evolution: its end-state is in panel B. In panel C, the free ends of three bilayers have merged into an equilibrium, Y-shaped junction.

Is it possible to replace the detailed hydrodynamic interaction with one that uses a constant coefficient drag coefficient law? The latter also exhibits particle self-assembly and avoids the computational cost of solving an additional mobility problem. Moreover, the constant coefficient case drag laws can closely replicate the hydrodynamic interaction case when particles are dispersed (see the supplementary material file Supplementary.pdf [local/web 394KB], section SM2.3). Nevertheless, numerical experiments show that the choice of dissipative mechanism is consequential to the time course. For example, Figure 7F and Figure 8B compare the two different end-states resulting from an identical initial configuration for a viscous fluid and for a constant drag law, respectively. The difference lies in the number of particles contained in the inner leaflet, and this has determined whether or not the bilayer closes.

**5. Boundary integral equation formulation.** In this section, we present an SKIE formulation for the exterior Dirichlet problem (1.3). The domain  $\Omega$  is the exterior domain, meaning that its complement  $\Omega^c$  (the collection of particles) is compact.

There are a number of numerical methods for solving the exterior problem (1.3). These include finite difference methods, finite element methods, and boundary integral equation (BIE) methods. The BIE methods are perhaps the most suitable since they represent the solution via layer potentials with an unknown density only on the boundary. This reduces the dimension of the problem by one and leads to a much smaller linear system. Another advantage is that the integral representation automatically satisfies the governing partial differential equation (PDE) and the boundary condition at infinity. Thus, there is no need to truncate the computational domain and impose artificial boundary conditions, as would be needed with the finite element and finite difference approaches. Finally, when combined with high-order quadratures and fast algorithms, such as the FMMs [31, 32], the BIE formulation leads to a high-order numerical algorithm with optimal computational complexity.

Before describing the method, we first consider whether the far-field condition in (1.3) is sufficient to determine a unique solution. As mentioned in section 1, the functional  $I[\cdot]$  has a unique minimizer in  $\mathcal{A}$ . The minimizer  $u$  satisfies  $0 \leq u(x) \leq 1$  for all  $x \in \Omega$ . To see why these bounds hold, consider a truncated version  $\tilde{u} = \max\{0, \min\{1, u\}\}$  of  $u$ . Because  $0 \leq f \leq 1$  on  $\Sigma$ ,  $\tilde{u} \in \mathcal{A}$ . Lastly,  $I[\tilde{u}] \leq I[u]$  by

inspection, and  $I[u] \leq I[\tilde{u}]$  by minimality of  $u$ . This implies that  $I[\tilde{u}] = I[u]$ , and since  $u$  is the unique minimizer, we have  $u = \tilde{u}$ .

To obtain a far-field decay condition, select a sufficiently large distance  $D > 0$  from  $\Omega^c$ . Let  $x$  be such that  $d(x, \Omega^c) > D$ . By a change of coordinates, we may assume that  $x$  is the origin  $(0, \dots, 0)$  and that  $\Omega^c$  lies in the set  $\{(x_1, \dots, x_n) : x_n \leq -D\}$ . In this coordinate system, consider the function

$$v_\epsilon(x_1, \dots, x_n) = \frac{\cosh(x_n/\rho)}{\cosh(D/\rho)} + \epsilon \sum_{i=1}^{n-1} \cosh(x_i/\rho), \quad \epsilon > 0.$$

Then  $-\rho^2 \Delta v_\epsilon + v_\epsilon = 0$  and  $v_\epsilon \geq 1$  on  $\Sigma$  (since  $x_n$  is less than  $-D$  there), and  $v_\epsilon \rightarrow \infty$  as  $|(x_1, \dots, x_n)| \rightarrow \infty$ . Next, consider the function  $g = v_\epsilon - u$ . We have  $g \geq 0$  on  $\Sigma$  and  $g \geq 0$  for all sufficiently large  $(x_1, \dots, x_n)$  (since  $v_\epsilon \rightarrow \infty$  and  $u$  is bounded everywhere between 0 and 1).

From the weak maximum principle [26, Cor. 3.2, assuming  $f \in C(\Sigma)$ ], we have  $g \geq 0$  in  $\Omega$ . It follows that  $v_\epsilon \geq u$  in  $\Omega$ . Finally, letting  $\epsilon \rightarrow 0$ , we conclude that

$$(5.1) \quad 0 \leq u(x) \leq v_\epsilon(x) < 2 \exp(-D/\rho)$$

as soon as  $\epsilon > 0$  is sufficiently small.

The problem (1.3) thus has at least one solution (vanishing at infinity), namely the variational one. But since the domain  $\Omega$  is noncompact, it is, in principle, possible that (1.3) has multiple solutions vanishing at infinity with different rates. The following Liouville-type result shows that this is not the case. In fact, we get uniqueness even if we replace the zero far-field condition with the power growth condition  $u = O(|x|^p)$  as  $x \rightarrow \infty$ .

LEMMA 5.1. *The exterior problem (1.3) has at most one solution.*

*Proof.* Suppose that (1.3) has two solutions  $u_1$  and  $u_2$ . Let  $w = u_1 - u_2$  and define

$$E(r) = \int_{\Omega \cap B_r} \frac{1}{2} w^2 dx, \quad E : [0, \infty) \rightarrow [0, \infty),$$

where  $B_r$  is the ball of radius  $r$  centered at the origin. Select  $r_0$  positive and sufficiently large so that  $\Omega^c \subset B_{r_0}$ .

The function  $E(r)$  is infinitely differentiable on  $(r_0, \infty)$  since any solution of (1.3) is smooth in  $\Omega$ . Using  $w = 0$  on  $\Sigma$  and (1.3), it follows that

$$(5.2) \quad E''(r) = \frac{n-1}{r} E'(r) + \frac{1}{\rho^2} E(r) + \int_{\Omega \cap B_r} |\nabla w|^2 dx, \quad r_0 < r < \infty.$$

Since  $E$  is nondecreasing, by definition, we get

$$E''(r) \geq \rho^{-2} E(r), \quad r_0 < r < \infty.$$

Let  $F(r) = \frac{1}{2} E(r_0) \exp((r - r_0)/\rho)$ . We claim that

$$(5.3) \quad F(r) \leq E(r), \quad r_0 \leq r < \infty.$$

To form the comparison argument, suppose to the contrary that  $E(r)$  is not everywhere greater than or equal to  $F(r)$ . Then  $E(r_0) > 0$  and there is  $r_* > r_0$  with

$E'(r_*) \leq F'(r_*)$  and  $F(r) < E(r)$  for  $r_0 \leq r < r_*$ . But then,

$$E'(r_*) \leq F'(r_*) = \int_{r_0}^{r_*} \rho^{-2} F(r) dr < \int_{r_0}^{r_*} \rho^{-2} E(r) dr \leq E'(r_*) - E'(r_0).$$

These inequalities are in contradiction since  $E'(r_0)$  is nonnegative.

Thus, if  $u_1$  and  $u_2$  are two solutions of (1.3), then according to (5.3) there is one of two possibilities: either  $E(r_0) = 0$  or one of the solutions has exponential growth. The vanishing condition  $u \rightarrow 0$  as  $x \rightarrow \infty$  rules out the latter case, and so  $E(r_0)$  must be zero. Since  $r_0$  was arbitrary,  $u_1$  and  $u_2$  are identical.  $\square$

In two dimensions, the equation  $-\rho^2 \Delta u + u = 0$  has the free-space Green's function (also called fundamental solution)

$$(5.4) \quad G(x, y) = \frac{1}{2\pi} K_0(|x - y|/\rho), \quad x, y \in \mathbb{R}^2,$$

where  $K_0$  is the zeroth-order modified Bessel function of the first kind [62]. For a Lipschitz domain  $\Omega$  in  $\mathbb{R}^2$  with boundary  $\Sigma$ , the space  $L^2(\Sigma)$  denotes all square integrable functions on  $\Sigma$ . Given a function  $\sigma \in L^2(\Sigma)$ , we define the single layer potential by the formula

$$(5.5) \quad \mathcal{S}[\sigma](x) = \int_{\Sigma} G(x, y) \sigma(y) ds_y,$$

and the double layer potential by the formula

$$(5.6) \quad \mathcal{D}[\sigma](x) = \int_{\Sigma} \frac{\partial G(x, y)}{\partial \nu(y)} \sigma(y) ds_y,$$

where  $\nu(y)$  is the unit outward normal vector with respect to  $\Omega^c$ . It is well known from classical potential theory [44] that the single layer potential is continuous and the double layer potential exhibits a jump across the boundary. To be more precise, when  $z$  approaches a point  $x \in \Sigma$  nontangentially, the limits of  $\mathcal{S}[\sigma]$  and  $\mathcal{D}[\sigma]$  exist and are given by the following formulas:

$$(5.7) \quad \lim_{z \rightarrow x^\pm} \mathcal{S}[\sigma](z) = \mathcal{S}[\sigma](x) = \int_{\Sigma} G(x, y) \sigma(y) ds_y$$

and

$$(5.8) \quad \lim_{z \rightarrow x^\pm} \mathcal{D}[\sigma](z) = \left( \pm \frac{1}{2} I + D \right) [\sigma](x) = \pm \frac{1}{2} \sigma(x) + \text{p.v.} \int_{\Sigma} \frac{\partial G(x, y)}{\partial \nu(y)} \sigma(y) ds_y$$

for almost every point  $x \in \Sigma$ . Here  $z \rightarrow x^\pm$  implies that  $z$  approaches  $x$  from the exterior(+) or the interior(-) of  $\Omega^c$ , respectively. It is also well known that both the single layer operator  $S : L^2(\Sigma) \rightarrow L^2(\Sigma)$  and the double layer operator  $D : L^2(\Sigma) \rightarrow L^2(\Sigma)$  are compact when the boundary  $\Sigma$  is  $C^1$ .

We will represent the solution to (1.3) with the double layer potential representation

$$(5.9) \quad u(x) = \mathcal{D}[\sigma](x).$$

The jump relation of the double layer potential (5.8) leads to the following BIE on the unknown density  $\sigma$ :

$$(5.10) \quad \frac{1}{2} \sigma(x) + D[\sigma](x) = f(x), \quad x \in \Sigma.$$



**Algorithm 5.1** Particle updates by exterior screened Laplace BVP.

- 
- 1: Set the particle centers  $\mathbf{a}_i \in \mathbb{R}^2$  and orientations  $\theta_i \in \mathbb{R}$ , boundary condition  $f(x)$  and time step size  $\Delta t$ .
  - 2: Determine the discretization on the boundary  $\Sigma$  and construct the double layer potential  $\mathcal{D}[\sigma](x)$ .
  - 3: **for**  $t = t_0 : t_{end}$  **do**
  - 4:   Use GMRES iterative method to solve the unknown density  $\sigma$  in (5.10).
  - 5:   Use the solved  $\sigma$  to obtain the screened Laplace equation solution  $u$  and calculate  $\nabla u$ .
  - 6:   Calculate intermolecular forces (2.2) and (2.16).
  - 7:   Use GMRES iterative method to solve the unknown density  $\mu$  in (4.6).
  - 8:   Solve mobility problem and update particle velocities  $\mathbf{v}_i$  and  $\omega_i$  in (4.7).
  - 9:   Update particle center positions  $\mathbf{a}_i$  and orientations  $\theta_i$ .
  - 10:   Update the marching time  $t = t_0 + \Delta t$ .
  - 11: **end for**
  - 12: **return**  $T$
- 

**THEOREM 5.2.** *Suppose that  $\rho$  is any positive real number. Then for any  $f \in L^2(\Sigma)$ , the SKIE (5.10) is uniquely solvable.*

*Proof.* By the Fredholm alternative [44], we need only show that the only solution to the homogeneous equation

$$(5.11) \quad \frac{1}{2}\sigma(x) + D[\sigma](x) = 0$$

is  $\sigma \equiv 0$ .

Consider the function  $u(x)$  defined by the formula (5.9). It is clear that  $u$  satisfies the equation  $-\rho^2 \Delta u + u = 0$  in both the exterior domain  $\Omega$  and the interior domain  $\Omega^c$ , and vanishes at infinity. By the uniqueness of the exterior Dirichlet problem (Lemma 5.1), we have  $u \equiv 0$  in  $\Omega$ . Hence,

$$(5.12) \quad \lim_{z \rightarrow x^+} \frac{\partial u(z)}{\partial \nu} = 0, \quad x \in \Sigma.$$

Since the normal derivative of the double layer potential is continuous across the boundary [44, gen. of Thm. 6.18], we have

$$(5.13) \quad \lim_{z \rightarrow x^-} \frac{\partial u(z)}{\partial \nu} = 0, \quad x \in \Sigma.$$

Hence,  $u$  in the interior domain  $\Omega^c$  is the solution to the interior Neumann problem

$$(5.14) \quad -\rho^2 \Delta u + u = 0, \quad u \in \Omega^c, \quad \frac{\partial u}{\partial \nu} = 0, \quad x \in \Sigma.$$

Applying Green's first identity, we obtain

$$(5.15) \quad \int_{\Omega^c} \rho^2 |\nabla u|^2 + u^2 dx = 0.$$

Thus we have  $u \equiv 0$  in  $\Omega^c$  as well. The jump relation of the double layer potential (5.8) leads to

$$(5.16) \quad \sigma(x) = \lim_{z \rightarrow x^+} u(z) - \lim_{z \rightarrow x^-} u(z) = 0, \quad x \in \Sigma,$$

which completes the proof.  $\square$

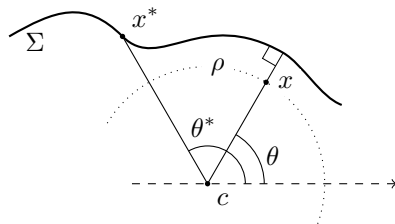


FIG. 9. Geometric situation of a single QBX expansion with sources along the collection of curves  $\Sigma$ , as used in (6.1) and (6.2). Note that the target point  $x$  will reside on  $\Sigma$  for the computation of the on-surface value of the layer potential.

*Remark 5.3.* As pointed out earlier, the screened Laplace equation can be viewed as the Helmholtz equation  $\Delta u + k^2 u = 0$  with pure imaginary  $k$ . When  $k$  is an arbitrary complex number, the so-called Brakhage–Werner representation [5] (also called the Burton–Miller representation [7] in acoustics) represents the solution to the Helmholtz equation via a linear combination of single and double layer potentials

$$(5.17) \quad u(x) = i\mathcal{S}[\sigma](x) + \mathcal{D}[\sigma](x).$$

It has been shown that the representation (5.17) leads to a uniquely solvable SKIE for any value of  $k \in \mathbb{C}$  [59]. Due to the exponential decay of the solution to our exterior problem (1.3), we are able to use the double layer potential alone to represent its solution and still achieve existence and uniqueness of the associated BIE (5.10).

We would like to point out that when  $\rho$  is very large, the formulation (5.17) may lead to a better conditioned linear system than (5.9). There are other SKIE formulations for this problem. For example, one may replace the single layer potential by a collection of point sources inside each particle, where the strength of the point source may be unknown or equal to the average value of the unknown density function on the boundary of each particle. We refer the reader to [29, 30, 36] for details.

**6. High-order quadrature and fast algorithms.** For the accurate and rapid evaluation of the layer potentials occurring in the previous section, we make use of Quadrature by Expansion, or QBX for short [39]. Here we briefly review the QBX scheme for the general Helmholtz kernel and note that the Yukawa kernel (5.4) is simply a special case of the Helmholtz kernel with pure imaginary wave number  $k$ . To do so, we cover a neighborhood of the source curve  $\Sigma$  with locally valid (local) expansions of the potential emanating from the entire source curve  $\Sigma$ . For a collection of on-surface target points  $(x_i)$ , expansion centers are chosen as  $c_i = x_i + \nu\eta_{x_i}$ , where  $\eta_x$  is a scaling factor connected to the local quadrature resolution. See [79] for details of the determination of  $\eta_x$ . Then, for target points  $x \in B(c_i, \eta_{x_i})$ , the layer potential may be evaluated as

$$(6.1) \quad \phi(x) = \sum_{l=-\infty}^{\infty} \alpha_l J_l(k\rho) e^{-il\theta},$$

where  $(\rho, \theta)$  denote the polar coordinates of the target point  $x$  with respect to the expansion center  $c$ , and  $J_l$  is the Bessel function of order  $l$  (see Figure 9). For the single layer potential  $S\sigma$ , the coefficients  $\alpha_l$  in the expansion (6.1) can be computed

analytically:

$$(6.2) \quad \alpha_l = \frac{i}{4} \int_{\Sigma} H_l^{(1)}(k|x^* - c|) e^{il\theta^*} \sigma(x^*) dx^*, \quad (l = -p, -p+1, \dots, p),$$

where  $(|x^* - c|, \theta^*)$  denote the polar coordinates of the point  $x^*$  with respect to  $c$ . These (now nonsingular) integrals for the coefficients  $\alpha_l$  are then computed by conventional high-order numerical quadrature. These formulas follow immediately from Graf's addition theorem [62, eq. (10.23.7)],

$$(6.3) \quad H_0^{(1)}(k|x - x^*|) = \sum_{l=-\infty}^{\infty} H_l^{(1)}(k|x^* - c|) e^{il\theta^*} J_l(k|x - c|) e^{-il\theta}.$$

This identity applies directly to the Yukawa potentials under consideration here, based on the fact that  $K_0(z) = (i\pi/2)H_0^{(1)}(iz)$ , cf. [62, eq. (10.27.8)]. Separation-of-variables results similar to Graf's addition theorem hold for Laplace potentials, allowing us to proceed analogously in that case [31]. The QBX procedure described above employs two means of approximation: the truncation of the series expansion, and the computation of the coefficients by numerical quadrature. We give an error result for QBX that accounts for both aspects. For the following result, we consider the case of the double layer and assume  $c = 0$  without loss of generality.

**THEOREM 6.1** (QBX truncation and quadrature errors, [16, Thm. 2.5 and eq. (4.6), generalized to  $k \in \mathbb{C}$ ]). *Suppose that  $\Gamma$  is a smooth, bounded curve embedded in  $\mathbb{R}^2$ , such that  $B_{\eta_x}(0) \cap \Gamma = \emptyset$ , but  $\rho e^{i\theta} \in \overline{B_{\eta_x}(0)} \cap \Gamma$ . Assume the geometry  $\Gamma$  is discretized using  $q$  point composite Gauss-Legendre panels of uniform length  $h$ . For  $k \neq 0$ ,  $N$  a positive integer, and  $\beta > 0$ , there are constants  $C'_{N,\beta,\Gamma}(k)$  and  $C''_{q,\Gamma}(k)$ , so that if  $\sigma \in C^{N,\beta}(\Gamma)$ , then*

$$(6.4) \quad \left| \lim_{r \rightarrow \rho^-} \int_{\Gamma} \frac{\partial G(re^{i\theta}, y)}{\partial \nu(y)} \sigma(y) ds(y) - \sum_{l=1-N}^{N-1} Q_q(\alpha_l) J_l(k\rho) e^{-il\theta} \right| \\ \leq C'_{N,\beta,\Gamma}(k) \rho^N \|\sigma\|_{C^{N,\beta}(\Gamma)} + C''_{q,\Gamma}(k) \frac{h^{2q}}{(4\rho)^{2q+1}} \|\sigma\|_{C^{2q}(\Gamma)}.$$

Here the coefficients  $\{\alpha_l\}$  are given analogously to (6.2), and  $Q_q(\alpha_l)$  denotes the approximation of the coefficient integral of (6.2) by Gaussian quadrature with  $q$  points.

The theorem makes several assumptions that may not be true of the geometry discretization in its original form, notably the assumption that the placed disks do not intersect with other geometry, or the requirement that source panels supply sufficient quadrature resolution not just for themselves, but also for adjacent panels (which masquerades in Theorem 6.1 as the assumption of equal panel sizes). All of these issues can be remedied by adequate refinement of the source geometry. An efficient, tree-based algorithm is available [79] to accomplish this.

To avoid quadratic scaling of the computational cost with the number of degrees of freedom, BIE methods require some form of acceleration, often through a variant of the Fast Multipole method (FMM) [8]. In the context of QBX, it is convenient to exploit the fact that the expansions produced as the output of the far-field stage of the FMM are the same ones employed by the quadrature method. However, without some care, loss of accuracy may occur [68]. We make use of the GIGAQBX fast

algorithm of [80] to obtain guaranteed accuracy at linearly scaling cost. This algorithm modifies the conventional FMM by forcing direct computation of interactions that may endanger the accuracy of the computed QBX expansion, in addition to a number of modifications to retain efficiency and linear scaling in that setting.

Another feature in GIGAQBX is the adaptive refinement activated when two or more source geometries get close to each other, causing near-singular evaluations of the boundary integral. The adaptive refinement is designed to continue until the expansion disks get out of the region of the source geometry [80]. Under the HAP, one might expect that many levels of refinement are needed when two particles are brought to near-contact. However, the steric potential (2.16) also acts to prevent particles from getting too close to each other.

With the use of the short-range repulsive potential, we found that the count of continuous refinements is at most three to five levels at each time step for simulations presented in this work. Moreover, if the target point is geometrically on the wrong side (e.g., the interior region for the exterior problem), the GIGAQBX approximates analytic continuation of the potential across the boundary  $\Gamma$ , leading to benign behavior even in degenerate cases.

Our simulation codes make use of the software package PYTENTIAL [40], which is, in turn, built upon FMMLIB [27] for some of its expansion and translation operator infrastructure.

**7. Conclusions.** Topological transitions of a lipid bilayer membrane, such as membrane fusion and fission, involve rearrangement of lipid molecules in the bilayer. Consequently, the well-known Helfrich free energy requires modification to account for lipid granularity to resolve the detailed lipid remodeling during membrane fusion or fission [61, 13, 72]. By using a modified Helfrich free energy with van der Waals repulsion and a hydrophobic potential for lipid tail-solvent interaction, Ryham et al. [72] calculated a least energy pathway of membrane fusion. Building on these results, the main motivation for the work presented here is to construct a hybrid continuum lipid model at the mesoscopic scales to capture both the lipid granularity and the long-range interaction during the self-assembly of lipid molecules and fusion/fission dynamics of a lipid bilayer membrane.

Our continuum coarse-grained model for lipids focuses on the hydrophobic interactions between lipid tails, and an SKIE formulation of the hydrophobic stress is derived and used for obtaining particle dynamics. We also show that the long-range HAP is nonpairwise, and thus requires special treatment within the coarse-grained model framework. The GIGAQBX scheme—an improved version of the QBX-FMM scheme with guaranteed accuracy—is used in the discretization, solver, and evaluation phases of the SKIE to achieve high accuracy and asymptotically optimal complexity. Simulation results of our model show that during the self-assembly process, coarse-grained lipid particles form structures (such as micelles and bilayers) that may further fuse together to form a single bilayer membrane. These results show that our approach can naturally capture the mesoscopic dynamics of membrane fusion/fission. Furthermore, we show that the hydrophobic interactions give rise to membrane curvature minimization, which is an indication of the origin of bending rigidity in a bilayer membrane.

It is straightforward to apply the numerical scheme developed in this paper to study particles of arbitrary shape. With slight algorithmic modification, the scheme can also accurately capture the collision dynamics that many researchers may regard as rather difficult to deal with.

We also illustrate that the lipid hydrodynamics under HAP gives rise to macroscopic mechanical properties of a lipid bilayer membrane that are consistent with other results in the literature. The flexibility of our hybrid approach allows us to consider a mixture of two lipid species and how spontaneous sorting (phase separation) of two lipid species leads to membrane fission, consistent with results from phase-field simulations [49]. Our future goal is to extend the current framework to a three-dimensional lipid system. We will incorporate fluctuating hydrodynamics into the boundary integral formulation to extract physical properties of the lipid bilayer membrane, such as membrane diffusivity, bending rigidity, and the surface tension. By modification of the interfacial labels, HAP can account for charged lipids and study their impact on elastic properties of a bilayer [20]. Since we have immersed the particles in a zero-Reynolds flow, it is possible to study the rheological properties of micelle networks in large particle simulations [50]. Finally, we also aim to investigate the continuum limit of our hybrid model and make a comparison with functionalized Canham–Helfrich models.

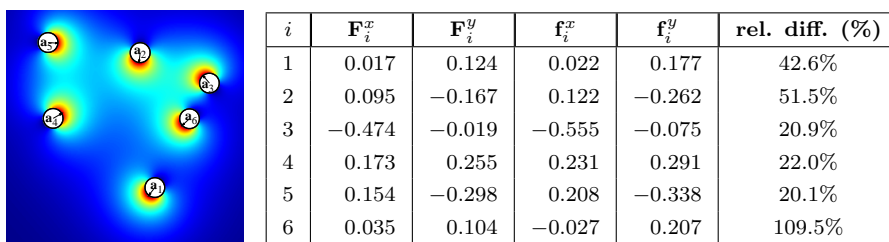


FIG. 10. The pseudocolor map shows a configuration of six randomly placed particles with random orientations. The table (in pN) provides values for the  $x$  and  $y$  components of force  $\mathbf{F}_i^{\{x,y\}}$  calculated from the HAP and the force  $\mathbf{f}_i^{\{x,y\}}$  calculated by assuming a pairwise potential (A.1). The rightmost column shows the relative difference  $\|\mathbf{F}_i - \mathbf{f}_i\|/\|\mathbf{F}_i\|$ .

**Appendix A. Pairwise potentials.** We show that pairwise potentials do not closely approximate the HAP. Consider the case of  $N$  many particles in general position and orientation. Their associated pairwise potential is

$$(A.1) \quad \sum_{i=1}^N \sum_{j>i} \phi_{ij},$$

where  $\phi_{ij}$  is the functional (1.1) evaluated on  $\Omega = \mathbb{R}^2 \setminus (P_i \cup P_j)$ . Differentiating (A.1) with respect to position  $\mathbf{a}_i$  yields the force

$$(A.2) \quad \mathbf{f}_i = \sum_{j \neq i} \mathbf{f}_{ij}, \quad \mathbf{f}_{ij} = -\nabla_{\mathbf{a}_i} \phi_{ij};$$

that is, we calculate  $\mathbf{f}_{ij}$  using (2.2) for a fluid domain containing only two particles,  $P_i$  and  $P_j$ , and then sum the results for  $j = 1, \dots, N, j \neq i$ . Finally, let  $\Phi$  be the HAP for all  $N$  particles, and calculate the hydrophobic force  $\mathbf{F}_i = -\nabla_{\mathbf{a}_i} \Phi$  using (2.2) over the fluid domain that contains all particles.

The table in Figure 10 compares the nonpairwise  $\mathbf{F}_i$  and pairwise  $\mathbf{f}_i$  forces for a sample particle configuration (Figure 10, pseudocolor map). The forces show significant differences for all six particles (Figure 10, rightmost column), suggesting that it is insufficient to use a pairwise potential to calculate HAP as formulated in the present

work. We note, however, that owing to the form of the free-space Green's function (5.4), the correlations between particles decays like  $\exp(-D/\rho)$  in their distance  $D$ . This makes it possible to localize interaction to tens of particles by setting a cutoff radius in the layer potential evaluations.

**Acknowledgments.** Part of this work was performed when S.-P. Fu, S. Jiang, A. Klöckner, and M. Wala were participating in the 2017 HKUST-ICERM workshop “Integral Equation Methods, Fast Algorithms and Their Applications to Fluid Dynamics and Materials Science.” The authors thank the anonymous referees, Joshua Schrier, Jasun Gong, John Lowengrub, and Jun Allard for valuable feedback.

## REFERENCES

- [1] C. BUNDLE AND A. WAGNER, *Second domain variation for problems with Robin boundary conditions*, J. Optim. Theory Appl., 167 (2015), pp. 430–463, <https://doi.org/10.1007/s10957-015-0801-1>.
- [2] S. BARTELS, G. DOLZMANN, AND R. H. NOCHETTO, *A finite element scheme for the evolution of orientational order in fluid membranes*, ESAIM: M2AN, 44 (2010), pp. 1–31, <https://doi.org/10.1051/m2an/2009040>.
- [3] D. BOAL, *Mechanics of the Cell*, 2nd ed., Cambridge University Press, Cambridge, UK, 2012.
- [4] J. F. BRADY AND G. BOSSIS, *Stokesian dynamics*, Ann. Rev. Fluid Mech., 20 (1988), pp. 111–157, <https://doi.org/10.1146/annurev.fl.20.010188.000551>.
- [5] H. BRAKHAGE AND P. WERNER, *Über das Dirichletsche Außenraumproblem für die Helmholtzsche Schwingungsgleichung*, Arch. Math., 16 (1965), pp. 325–329, <https://doi.org/10.1007/BF01220037>.
- [6] S. BURGER, T. FRAUNHOLZ, C. LEIRER, R. H. W. HOPPE, A. WIXFORTH, M. A. PETER, AND T. FRANKE, *Comparative study of the dynamics of lipid membrane phase decomposition in experiment and simulation*, Langmuir, 29 (2013), pp. 7565–7570, <https://doi.org/10.1021/la401145t>.
- [7] A. J. BURTON AND G. F. MILLER, *The application of integral equation methods to the numerical solution of some exterior boundary-value problems: A discussion on numerical analysis of partial differential equations*, Proc. Roy. Soc. London Ser. A, 323 (1971), pp. 201–210.
- [8] J. CARRIER, L. GREENGARD, AND V. ROKHLIN, *A fast adaptive multipole algorithm for particle simulations*, SIAM J. Sci. Stat. Comput., 9 (1988), pp. 669–686, <https://doi.org/10.1137/0909044>.
- [9] P. CHLANDA, E. MEKHEDOV, H. WATERS, C. L. SCHWARTZ, E. R. FISCHER, R. J. RYHAM, F. S. COHEN, P. S. BLANK, AND J. ZIMMERBERG, *The hemifusion structure induced by influenza virus haemagglutinin is determined by physical properties of the target membranes*, Nat. Microbio., 1 (2016), 16050.
- [10] F.-X. CONTRERAS, L. SÁNCHEZ-MAGRANER, A. ALONSO, AND F. M. GOÑI, *Transbilayer (flip-flop) lipid motion and lipid scrambling in membranes*, in Frontiers in Membrane Biochemistry, FEBS Letters, 584 (2010), pp. 1779–1786, <https://doi.org/10.1016/j.febslet.2009.12.049>.
- [11] I. R. COOKE AND M. DESERNO, *Solvent-free model for self-assembling fluid bilayer membranes: Stabilization of the fluid phase based on broad attractive tail potentials*, J. Chem. Phys., 123 (2005), 224710, <https://doi.org/10.1063/1.2135785>.
- [12] S. DAI AND K. PROMISLOW, *Geometric evolution of bilayers under the functionalized Cahn-Hilliard equation*, Proc. R. Soc. Lond. Ser. A Math. Phys. Eng. Sci., 469 (2013), 20120505.
- [13] S. DAI AND K. PROMISLOW, *Competitive geometric evolution of amphiphilic interfaces*, SIAM J. Math. Anal., 47 (2015), pp. 347–380, <https://doi.org/10.1137/130941432>.
- [14] D. E. DISCHER AND A. EISENBERG, *Polymer vesicles*, Science, 297 (2002), pp. 967–973.
- [15] W. A. DUCKER AND D. MASTROPIETRO, *Forces between extended hydrophobic solids: Is there a long-range hydrophobic force?*, Curr. Opin. Colloid Interface Sci., 22 (2016), pp. 51–58, <https://doi.org/10.1016/j.cocis.2016.02.006>.
- [16] C. L. EPSTEIN, L. GREENGARD, AND A. KLÖCKNER, *On the convergence of local expansions of layer potentials*, SIAM J. Numer. Anal., 51 (2013), pp. 2660–2679, <https://doi.org/10.1137/120902859>.
- [17] J. C. ERIKSSON, S. LJUNGGREN, AND P. M. CLAESON, *A phenomenological theory of long-range hydrophobic attraction forces based on a square-gradient variational approach*, J. Chem. Soc., Faraday Trans. 2, 85 (1989), pp. 163–176, <https://doi.org/10.1039/F29898500163>.

- [18] E. EVANS, V. HEINRICH, F. LUDWIG, AND W. RAWICZ, *Dynamic tension spectroscopy and strength of biomembranes*, Biophys. J., 85 (2003), pp. 2342–2350, [https://doi.org/10.1016/S0006-3495\(03\)74658-X](https://doi.org/10.1016/S0006-3495(03)74658-X).
- [19] L. C. EVANS, *Partial Differential Equations*, 2nd ed., Grad. Stud. Math. 19, AMS, Providence, RI, 2001.
- [20] H. A. FAIZI, S. L. FREY, J. STEINKÜLER, R. DIMOVA, AND P. M. VLAHOVSKA, *Bending rigidity of charged lipid bilayer membranes*, Soft Matter, 15 (2019), pp. 6006–6013.
- [21] W. FENG, Z. GUAN, J. LOWENGRUB, C. WANG, S. WISE, AND Y. CHEN, *A uniquely solvable, energy stable numerical scheme for the functionalized Cahn-Hilliard equation and its convergence analysis*, J. Sci. Comput., 76 (2018), pp. 1938–1967.
- [22] C. FRANÇOIS-MARTIN, J. E. ROTHMAN, AND F. PINCET, *Low energy cost for optimal speed and control of membrane fusion*, Proc. Natl. Acad. Sci. USA, 114 (2017), pp. 1238–1241, <https://doi.org/10.1073/pnas.1621309114>.
- [23] S.-P. FU, Z. PENG, H. YUAN, R. KFOURY, AND Y.-N. YOUNG, *Lennard-Jones type pair-potential method for coarse-grained lipid bilayer membrane simulations in LAMMPS*, Comput. Phys. Commun., 210 (2017), pp. 193–203, <https://doi.org/10.1016/j.cpc.2016.09.018>.
- [24] A. J. GARCÍA-SÁEZ, S. CHIANTIA, AND P. SCHWILLE, *Effect of line tension on the lateral organization of lipid membranes*, J. Biol. Chem., 282 (2007), pp. 33537–33544, <https://doi.org/10.1074/jbc.M706162200>.
- [25] P. GERA AND D. SALAC, *Cahn-Hilliard on surfaces: A numerical study*, Appl. Math. Lett., 73 (2017), pp. 56–61, <https://doi.org/10.1016/j.aml.2017.02.021>.
- [26] D. GILBARG AND N. S. TRUDINGER, *Elliptic Partial Differential Equations of Second Order*, Springer-Verlag, Berlin, 2001.
- [27] Z. GIMBUTAS AND L. GREENGARD, *Fmmlib2d*, <https://github.com/zgimbutas/fmmlib2d> (accessed June 2018).
- [28] G. GOMPPER AND M. SCHICK, *Correlation between structural and interfacial properties of amphiphilic systems*, Phys. Rev. Lett., 65 (1990), pp. 1116–1119.
- [29] A. GREENBAUM, L. GREENGARD, AND G. B. MCFADDEN, *Laplace's equation and the Dirichlet-Neumann map in multiply connected domains*, J. Comput. Phys., 105 (1993), pp. 267–278.
- [30] L. GREENGARD, M. C. KROPINSKI, AND A. MAYO, *Integral equation methods for Stokes flow and isotropic elasticity in the plane*, J. Comput. Phys., 125 (1996), pp. 403–414.
- [31] L. GREENGARD AND V. ROKHLIN, *A fast algorithm for particle simulations*, J. Comput. Phys., 73 (1987), pp. 325–348.
- [32] L. F. GREENGARD AND J. HUANG, *A new version of the fast multipole method for screened Coulomb interactions in three dimensions*, J. Comput. Phys., 180 (2002), pp. 642–658.
- [33] W. HELFRICH, *Elastic properties of lipid bilayers: Theory and possible experiments*, Z. Naturforsch. C, 28 (1973), pp. 693–703.
- [34] J. HU, Y. SHIBATA, C. VOSS, T. SHEMES, Z. LI, M. COUGHLIN, M. M. KOZLOV, T. A. RAPOPORT, AND W. A. PRINZ, *Membrane proteins of the endoplasmic reticulum induce high-curvature tubules*, Science, 319 (2008), pp. 1247–1250, <https://doi.org/10.1126/science.1153634>.
- [35] J. N. ISRAELACHVILI, S. MARČELJA, AND R. G. HORN, *Physical principles of membrane organization*, Q. Rev. Biophys., 13 (1980), pp. 121–200, <https://doi.org/10.1017/S0033583500001645>.
- [36] S. JIANG, M. RACHH, AND Y. XIANG, *An efficient high order method for dislocation climb in two dimensions*, Multiscale Model. Simul., 15 (2017), pp. 235–253, <https://doi.org/10.1137/16M1081920>.
- [37] M. JURÁSEK AND R. VÁCHA, *Self-assembled clusters of patchy rod-like molecules*, Soft Matter, 13 (2017), pp. 7492–7497, <https://doi.org/10.1039/C7SM01384A>.
- [38] I. KABELKA AND R. VÁCHA, *Optimal hydrophobicity and reorientation of amphiphilic peptides translocating through membrane*, Biophys. J., 115 (2018), pp. 1045–1054, <https://doi.org/10.1016/j.bpj.2018.08.012>.
- [39] A. KLÖCKNER, A. BARNETT, L. GREENGARD, AND M. O'NEIL, *Quadrature by expansion: A new method for the evaluation of layer potentials*, J. Comput. Phys., 252 (2013), pp. 332–349.
- [40] A. KLÖCKNER AND M. WALA, *Pyntential: A software package for the evaluation of layer potentials*, <https://github.com/inducer/pyntential> (accessed June 2018).
- [41] D. I. KOPELEVICH AND J. F. NAGLE, *Correlation between length and tilt of lipid tails*, J. Chem. Phys., 143 (2015), 154702, <https://doi.org/10.1063/1.4932971>.
- [42] M. M. KOZLOV, *Determination of lipid spontaneous curvature from X-ray examinations of inverted hexagonal phases*, in Methods in Membrane Lipids, Methods Mol. Biol. 400, Humana Press, Totowa, NJ, 2007, pp. 355–366.
- [43] N. KRAITZMAN AND K. PROMISLOW, *Pearling bifurcations in the strong functionalized Cahn–*

- Hilliard free energy*, SIAM J. Math. Anal., 50 (2018), pp. 3395–3426, <https://doi.org/10.1137/16M1108406>.
- [44] R. KRESS, *Linear Integral Equations*, Appl. Math. Sci. 82, Springer, New York, 2014.
  - [45] P. I. KUZMIN, S. A. AKIMOV, Y. A. CHIZMADZHEV, J. ZIMMERBERG, AND F. S. COHEN, *Line tension and interaction energies of membrane rafts calculated from lipid splay and tilt*, Biophys. J., 88 (2005), pp. 1120–1133, <https://doi.org/10.1529/biophysj.104.048223>.
  - [46] P. LAX, *Functional Analysis*, Pure Appl. Math. (N.Y.), John Wiley & Sons, New York, 2002.
  - [47] L. G. LEAL, *Advanced Transport Phenomena: Fluid Mechanics and Convective Transport Processes*, Cambridge Ser. Chem. Eng., Cambridge University Press, Cambridge, UK, 2007, <https://doi.org/10.1017/CBO9780511800245>.
  - [48] Q. LIN, E. E. MEYER, M. TADMOR, J. N. ISRAELACHVILI, AND T. L. KUHL, *Measurement of the long- and short-range hydrophobic attraction between surfactant-coated surfaces*, Langmuir, 21 (2005), pp. 251–255, <https://doi.org/10.1021/la048317q>.
  - [49] J. S. LOWENGRUB, A. RATZ, AND A. VOIGT, *Phase-field modeling of the dynamics of multi-component vesicles: Spinodal decomposition, coarsening, budding, and fission*, Phys. Rev. E (3), 79 (2009), 031926.
  - [50] V. LUTZ-BUENO, R. PASQUINO, M. LIEBI, J. KOHLBRECHER, AND P. FISCHER, *Viscoelasticity enhancement of surfactant solutions depends on molecular conformation: Influence of surfactant headgroup structure and its counterion*, Langmuir, 32 (2016), pp. 4239–4250.
  - [51] J. L. MACCALLUM AND D. P. TIELEMAN, *Hydrophobicity scales: A thermodynamic looking glass into lipid-protein interactions*, Trends Biochem. Sci., 36 (2011), pp. 653–662.
  - [52] S. J. MARRINK, H. J. RISSELADA, S. YEFIMOV, D. P. TIELEMAN, AND A. H. DE VRIES, *The martini force field: Coarse grained model for biomolecular simulations*, J. Phys. Chem. B, 111 (2007), pp. 7812–7824.
  - [53] L. I. MENSHIKOV, P. L. MENSHIKOV, AND P. O. FEDICHEV, *Phenomenological model of hydrophobic and hydrophilic interactions*, J. Exp. Theor. Phys., 125 (2017), pp. 1173–1188, <https://doi.org/10.1134/S1063776117120056>.
  - [54] E. E. MEYER, K. J. ROSENBERG, AND J. ISRAELACHVILI, *Recent progress in understanding hydrophobic interactions*, Proc. Natl. Acad. Sci. USA, 103 (2006), pp. 15739–15746, <https://doi.org/10.1073/pnas.0606422103>.
  - [55] M. MIKUCKI AND Y. ZHOU, *Curvature-driven molecular flow on membrane surface*, SIAM J. Appl. Math., 77 (2017), pp. 1587–1605, <https://doi.org/10.1137/16M1076551>.
  - [56] J. F. NAGLE, *Experimentally determined tilt and bending moduli of single-component lipid bilayers*, Chem. Phys. Lipids, 205 (2017), pp. 18–24.
  - [57] J. F. NAGLE, *Mechanical properties of lipid bilayers*, Eur. Pharm. J., 64 (2017), pp. 22–23.
  - [58] J. F. NAGLE, M. S. JABLIN, S. TRISTRAM-NAGLE, AND K. AKABORI, *What are the true values of the bending modulus of simple lipid bilayers?*, Chem. Phys. Lipids, 185 (2015), pp. 3–10, <https://doi.org/10.1016/j.chemphyslip.2014.04.003>.
  - [59] J. C. NÉDÉLEC, *Acoustic and Electromagnetic Equations: Integral Representations for Harmonic Problems*, Appl. Math. Sci. 144, Springer, New York, 2001.
  - [60] H. NOGUCHI, *Solvent-free coarse-grained lipid model for large-scale simulations*, J. Chem. Phys., 134 (2011), 055101, <https://doi.org/10.1063/1.3541246>.
  - [61] T. OHTA AND K. KAWASAKI, *Equilibrium morphology of block copolymer melts*, Macromolecules, 19 (1986), pp. 2621–2632, <https://doi.org/10.1021/ma00164a028>.
  - [62] F. W. J. OLVER, A. B. OLDE DAALHUIS, D. W. LOZIER, B. I. SCHNEIDER, R. F. BOISVERT, C. W. CLARK, B. R. MILLER, B. V. SAUNDERS, H. S. COHL, AND M. A. MCCLAIN, EDs., *NIST Digital Library of Mathematical Functions*, <http://dlmf.nist.gov> (accessed May 2010).
  - [63] V. PARSEGAN AND R. RAND, *Chapter 13 - Interaction in membrane assemblies*, in Structure and Dynamics of Membranes, R. Lipowsky and E. Sackmann, eds., Handbook of Biological Physics 1, North-Holland, 1995, pp. 643–690, [https://doi.org/10.1016/S1383-8121\(06\)80006-0](https://doi.org/10.1016/S1383-8121(06)80006-0).
  - [64] V. A. PARSEGAN AND B. W. NINHAM, *Temperature-dependent van der Waals forces*, Biophys. J., 10 (1970), pp. 664–674.
  - [65] A. D. PETELSKA, *Interfacial tension of bilayer lipid membranes*, Cent. Eur. J. Chem., 10 (2012), pp. 16–26, <https://doi.org/10.2478/s11532-011-0130-7>.
  - [66] S. PLIMPTON, P. CROZIER, AND A. THOMPSON, *LAMMPS-large-scale atomic/molecular massively parallel simulator*, Sandia National Laboratories, 18 (2007), 43.
  - [67] M. RACHH, *Integral Equation Methods for Problems in Electrostatics, Elastostatics and Viscous Flow*, Ph.D. thesis, New York University, New York, 2015.
  - [68] M. RACHH, A. KLÖCKNER, AND M. O’NEIL, *Fast algorithms for quadrature by expansion I: Globally valid expansions*, J. Comput. Phys., 345 (2017), pp. 706–731, <https://doi.org/10.1016/j.jcp.2017.04.062>.



- [69] B. REN, A. RUDITSKIY, J. H. K. SONG, AND I. KRETZSCHMAR, *Assembly behavior of iron oxide-capped Janus particles in a magnetic field*, *Langmuir*, 28 (2012), pp. 1149–1156, <https://doi.org/10.1021/la203969f>.
- [70] E. RIDEAU, R. DIMOVA, P. SCHWILLE, F. R. WURM, AND K. LANDFESTER, *Liposomes and polymersomes: A comparative review towards cell mimicking*, *Chem. Soc. Rev.*, 47 (2018), pp. 8572–8610, <https://doi.org/10.1039/C8CS00162F>.
- [71] B. ROZYCKI AND R. LIPOWSKY, *Spontaneous curvature of bilayer membranes from molecular simulations: Asymmetric lipid densities and asymmetric adsorption*, *J. Chem. Phys.*, 142 (2015), 054101, <https://doi.org/10.1063/1.4906149>.
- [72] R. J. RYHAM, T. S. KLOTZ, L. YAO, AND F. S. COHEN, *Calculating transition energy barriers and characterizing activation states for steps of fusion*, *Biophys. J.*, 110 (2016), pp. 1110–1124.
- [73] M. SCHIFFER, *Variation of domain functionals*, *Bull. Amer. Math. Soc.*, 60 (1954), pp. 303–328.
- [74] B. SEGUIN AND E. FRIED, *Calculating the bending moduli of the Canham-Helfrich free-energy density*, *J. Math. Biol.*, 68 (2014), pp. 345–361.
- [75] B. SEGUIN AND E. FRIED, *Microphysical derivation of the Canham-Helfrich free-energy density*, *J. Math. Biol.*, 68 (2014), pp. 647–665.
- [76] M. M. TERZI AND M. DESERNO, *Novel tilt-curvature coupling in lipid membranes*, *J. Chem. Phys.*, 147 (2017), 084702, <https://doi.org/10.1063/1.4990404>.
- [77] M. M. TERZI AND M. DESERNO, *Lipid membranes: From self-assembly to elasticity*, in *The Role of Mechanics in the Study of Lipid Bilayers*, D. Steigman, ed., CISM 577, Springer, Cham, 2018, pp. 105–166, [https://doi.org/10.1007/978-3-319-56348-0\\_3](https://doi.org/10.1007/978-3-319-56348-0_3).
- [78] R. M. VENABLE, F. L. BROWN, AND R. W. PASTOR, *Mechanical properties of lipid bilayers from molecular dynamics simulation*, *Chem. Phys. Lipids*, 192 (2015), pp. 60–74, <https://doi.org/10.1016/j.chemphyslip.2015.07.014>.
- [79] M. WALA AND A. KLÖCKNER, *A fast algorithm for quadrature by expansion in three dimensions*, *J. Comput. Phys.*, 388 (2019), pp. 655–689.
- [80] M. WALA AND A. KLÖCKNER, *A fast algorithm with error bounds for quadrature by expansion*, *J. Comput. Phys.*, 374 (2018), pp. 135–162, <https://doi.org/10.1016/j.jcp.2018.05.006>.
- [81] Y. WANG, J. K. SIGURDSSON, E. BRANDT, AND P. ATZBERGER, *Dynamic implicit-solvent coarse-grained models of lipid bilayer membranes: Fluctuating hydrodynamics thermostat*, *Phys. Rev. E*, 88 (2013), 023301.
- [82] J. YOO, M. B. JACKSON, AND Q. CUI, *A comparison of coarse-grained and continuum models for membrane bending in lipid bilayer fusion pores*, *Biophys. J.*, 104 (2013), pp. 841–852.